Mon. Not. R. Astron. Soc. **388,** 1899–1903 (2008) doi:10.1111/j.1365-2966.2008.13532.x

Observation of multiple sausage oscillations in cool post-flare loop

A. K. Srivastava,[1]★ T. V. Zaqarashvili,[2] W. Uddin,[1] B. N. Dwivedi[3] and Pankaj Kumar[1]†

[1]*Aryabhatta Research Institute of Observational Sciences (ARIES), Nainital-263129, India*
[2]*Abastumani Astrophysical Observatory at I. Chavchavadze State University, Al Kazbegi ave. 2a, 0160 Tbilisi, Georgia*
[3]*Department of Applied Physics, Institute of Technology, Banaras Hindu University, Varanasi-221005, India*

Accepted 2008 June 3. Received 2008 May 7; in original form 2008 March 11

ABSTRACT

Using simultaneous high spatial (1.3 arcsec) and temporal (5 and 10 s) resolution Hα observations from the 15 cm Solar Tower Telescope at Aryabhatta Research Institute of Observational Sciences (ARIES), we study the oscillations in the relative intensity to explore the possibility of sausage oscillations in the chromospheric cool post-flare loop. We use the standard wavelet tool, and find the oscillation period of $\approx$587 s near the loop apex, and $\approx$349 s near the footpoint. We suggest that the oscillations represent the fundamental and the first harmonics of the fast-sausage waves in the cool post-flare loop. Based on the period ratio $P_1/P_2 \sim 1.68$, we estimate the density scaleheight in the loop as $\sim$17 Mm. This value is much higher than the equilibrium scaleheight corresponding to Hα temperature, which probably indicates that the cool post-flare loop is not in hydrostatic equilibrium. Seismologically estimated Alfvén speed outside the loop is $\sim$300–330 km s^{-1}. The observation of multiple oscillations may play a crucial role in understanding the dynamics of lower solar atmosphere, complementing such oscillations already reported in the upper solar atmosphere (e.g. hot flaring loops).

Key words: MHD – waves – Sun: chromosphere – Sun: flares – Sun: oscillations.

1 INTRODUCTION

The coupling of complex magnetic field and plasma generates a variety of magnetohydrodynamic (MHD) waves and oscillations in various solar structures. These MHD waves and oscillations are one of the important candidates for coronal heating and solar wind acceleration. The idea of exploiting observed oscillations as a diagnostic tool for determining the physical conditions of the coronal plasma was first suggested by Roberts, Edwin & Benz (1984). Until recently, the application of this idea has been marked by the lack of high-quality observations of coronal oscillations. However, this situation has changed dramatically, especially due to space-based observations by the Solar and Heliospheric Observatory (SOHO), the Transition Region and Coronal Explorer (TRACE) and, most recently, with the high-resolution spectra from the Hinode spacecraft. The fast-kink wave is most frequently observed mode as it can be directly detected by periodic spatial displacement of the coronal loop axis (Aschwanden et al. 1999; Nakariakov et al. 1999; Wang & Solanki 2004). Using temporal series image data from the Coronal Diagnostic Spectrometer (CDS)/SOHO, recently O'Shea et al. (2007) have found the first evidence of fast-kink standing oscillations in the cool transition region loops as well. On the other hand, the fast-MHD sausage wave causes the variation of pressure and magnetic field in a coronal loop and therefore can be observed as intensity oscillations or periodic modulation of coronal radio emission (Nakariakov, Melnikov & Reznikova 2003). Recently, Srivastava et al. (2008) have reported the signature of the leakage of chromospheric magnetoacoustic oscillations into the corona near the south pole. These observations provide a basis for the estimation of coronal plasma properties (Nakariakov & Ofman 2001).

Recently, Verwichte et al. (2004) have detected interesting phenomenon of simultaneous existence of fundamental and first harmonics of fast-kink oscillations (see also De Moortel & Brady 2007; Van Doorsselaere, Nakariakov & Verwichte 2007). However, the ratio between the periods of fundamental and first harmonics P_1/P_2 was significantly shifted from 2, which later was explained as a result of longitudinal density stratification in the loop (Andries, Arregui & Goossens 2005; McEwan et al. 2006). The rate of the shift allows us to estimate the density scaleheight in coronal loops, which can be a few times larger compared to its hydrostatic value (Aschwanden, Nightingale & Alexander 2000).

In this paper, we report the first evidence of fundamental and first harmonics of fast sausage oscillations in cool post-flare loop. We use high spatial (1.3 arcsec) and temporal (5 and 10 s) resolution Hα observations from the 15 cm Solar Tower Telescope at Aryabhatta Research Institute of Observational Sciences (ARIES), Nainital, India, to study the oscillations in the relative intensity.

★E-mail: aks@aries.ernet.in
†Send off-print request to Dr. A.K. Srivastava, ARIES, Manora Peak, Nainital-263 129, India.

Using the standard wavelet tool, we find multiple oscillation periods at different parts of the loop, which are interpreted as the fundamental and first harmonics of the fast-sausage mode. In Section 2, we describe the observations and data reduction. We describe the wavelet analysis in Section 3. In Section 4, we present our theoretical model and its link to coronal seismology. We present results and discussion in the last section.

2 OBSERVATIONS AND DATA REDUCTION

The observations of post-flare loops have been carried out with 15 cm, f/15 Coudé Solar Tower Telescope at ARIES, Nainital, India, equipped with Bernhard Hale Hα filter ($\lambda = 6563$ Å and P.B. 0.5/0.7 Å) and PXL Photometric CCD camera. The filter is a birefringent Lyot-type filter, tunable $\pm$ 1 Å from central wavelength (6563 Å) with the step of 0.1 Å. During our observations, we set it at central wavelength 6563 Å with passband 0.5 Å. The image size has been enlarged by a factor of 2 using a Barlow lens. The 512 $\times$ 512 pixel, 12-bit frame-transfer CCD camera has a square pixel of 15 μm^2 corresponding to a 0.65 arcsec pixel size. The spatial resolution of our observations is 1.30 arcsec. The read-out noise for the system is 31 e^- with a gain of 44.1 e^- ADU^{-1}. Dark current of the camera is 56 e^- s^{-1}. The dark current is integrated over the 512 $\times$ 512 pixel. The camera controller of the system has a variable read-out rate from 0.5 to 2 MHz. The variable read-out rate of our CCD provides us the facility of fast imaging of the flares at different rates. In these observations, we have used a constant read-out rate of 2 MHz. The CCD chip (EEV 37) is cooled up to -25°C using the liquid cooling system.

We analyse the post-flare loop system between 01:00:52 UT and 01:58:28 UT on 2001 May 2, at a cadence of 5 and 10 s with an exposure time of 30 ms. The post-flare loop system was associated with M1.8 class limb flare which occurred in National Oceanic and Atmospheric Administration (NOAA) active region AR 9433 (N15, W88). Since the temporal evolution/changes were very fast during the onset of the post-flare loop system, we took fast sequence of images with 5 s cadence. As time progresses in the gradual/decay phase, the temporal changes become slow compared to initial phase of post-flare loop system. So, we took the sequence of images with 10 s cadence. Hence, there are two cadences, initially 5 s and later on 10 s. We have started our fast imaging with 5 s cadence on 00:52:11 UT. In the beginning of our observations, the flare was in decay phase and was enveloped by complex post-flare loop system. Hence, we were unable to select the distinct loop initially. When the post-flare loop system became more relaxed and distinctly visible around 01:00:52 UT, we have selected images of a clearly visible loop for our study after 01:00:52 UT. In our analysis, first 92 frames were with 5 s cadence, while the rest of the frames were with 10 s cadence. The total number of the frames used in this study is 390. We find that the post-flare loop system shows the similar structure/evolution in SOHO/Extreme-ultraviolet Imaging Telescope (EIT) (171, 195, 284, 304 Å) and Hα observations. The post-flare loop system which was visible at higher temperature (6.0×10^4 K $- 3.0 \times 10^6$ K) with EIT has also seen in Hα at the lower temperature ($\approx 10^4$ K) after its cooling. In Fig. 1 (top panel), the image of the post-flare loop system in high-resolution Hα has been shown, while the same loop system observed with SOHO/EIT Fe IX/X 171 Å has been shown in the bottom panel. Both images show the clear shape of the dynamic post-flare loop that we have selected. The loop top and footpoint of this prominent loop are marked by arrows in these two images. Since the spatial resolution of our Hα observations is high in comparison to the SOHO/EIT, we cannot see the features in EIT as sharp as in Hα image.

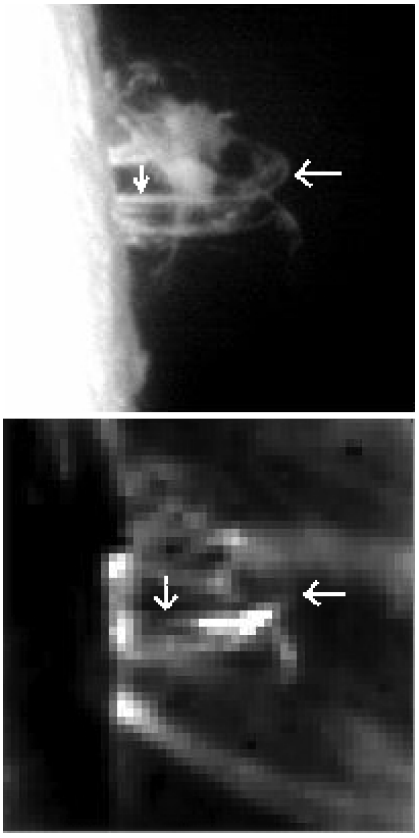

Figure 1. The Hα post-flare loops as observed by 15 cm Solar Tower Telescope at ARIES, Nainital, India. The FOV is 200 $\times$ 200 pixel (or 130 $\times$ 130 arcsec^2) (top panel). The aligned SOHO/EIT Fe IX/X 171 Å image of the same loop system is presented in the bottom panel.

We have estimated the length of the selected loop in Hα and SOHO/EIT Fe IX/X 171 Å images. We find the lengths $\sim$97 and $\sim$100 Mm in the Hα and EUV images, respectively. The estimated loop lengths at two wavelengths are almost equal which clearly shows the presence of the same loop at different temperatures. The lower atmosphere may not necessarily be an optically thin atmosphere, and many bright structures cross each other in the field of view. However, the chromospheric post-flare loop system is very complex and dynamic in itself, instead of being simpler and static. The features are temporally changing very fast in the observations. So, we carefully selected the image frames of the clearly visible loop in order to study the oscillations. The sky condition was very good during the observations. Several dark and flat-field images have also been taken to calibrate the Hα images. Using IRAF and SSWIDL software, the image processing has been performed. The details of the instrument can be obtained from Ali et al. (2007) and Joshi, Chandra & Uddin (2003).

3 WAVELET ANALYSIS

We use the Morlet wavelet tool to produce the power spectrum of oscillations in Hα. The Morlet wavelet suffers from the edge effect of time series data. This effect is significant in regions defined as cone of influence (COI). The details of wavelet procedure, its noise filtering, COI effects, etc. are given in Torrence & Compo (1998). The randomization technique evaluates the peak power in

the global wavelet spectrum, which is just the average peak power over time and similar to a smoothed Fourier power spectrum. This technique compares it to the peak powers evaluated from the $n!$ equally likely permutations of the time series data, assuming that n values of measured intensities are independent of n measured times if there is no periodic signal. The proportion of permutations, which gives the value greater or equal to the original peak power of the time series, will provide the probability of no periodic component (p). The percentage probability of periodic components presented in the data will be $(1 - p) \times 100$, and 95 per cent is the lowest acceptable probability for real oscillations. We set 200 permutations for the reliable estimation of p, and hence the probability of real oscillations. The details of the randomization technique to obtain the statistically significant real oscillation periods are given by Linnell Nemec & Nemec (1985) and O'Shea et al. (2001). We do not remove any upper/longer period intervals and associated powers of our time series data during the wavelet analysis. We choose the 'running average' option of O'Shea's wavelet tool and smoothen the original signal by window width 60. Average smoothing process is used to reduce the noise in the original signal in order to get a real periodicity, and it is based on the low pass filtering methods. The 'Running Average' process smoothens the original signal by the defined scalar width. This process uses the 'SMOOTH' subroutine available with IDL tool kit. The SMOOTH function returns a copy of array smoothed with a boxcar average of the specified width. The result has the same type and dimensions as array. The fitted signal is then subtracted from the original signal, and gives the resultant signal for the wavelet analysis. The maximum allowed period from COI, where edge effect is more effective, is 1259 s. Hence, the power reduces substantially beyond this threshold. In our wavelet analysis, we only consider the power peaks and corresponding real periods below this threshold. We performed the wavelet analysis at different parts (near the apex and footpoint) of the selected loop. We have chosen a location of $(X, Y) =$ (133th pixel, 117th pixel) near the apex, where the dominant periodicity is ≈587 s with the probability of ≈99–100 per cent (Fig. 2). We have again chosen a location of $(X, Y) =$ (58th pixel, 104th pixel) near the footpoint of the same loop, where the dominant oscillation period is ≈349 s with

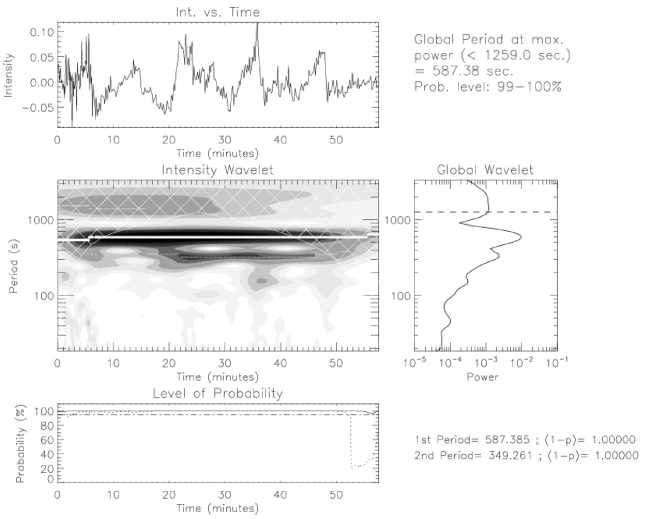

Figure 2. The wavelet result for Hα 6563 Å near the loop apex. The top panel shows the variation of intensity, the wavelet power spectrum is given in the middle panel and the probability is given in the bottom panel. The light curve is from the loop apex $(X, Y) =$ (133th pixel, 117th pixel) and is smoothed by window width 60.

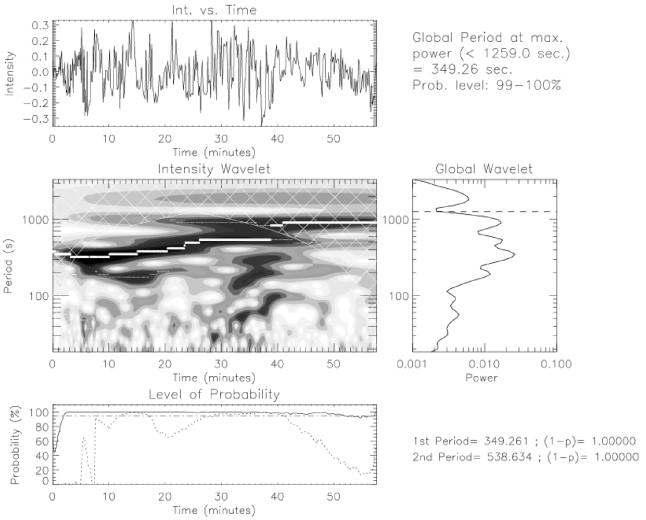

Figure 3. The wavelet result for Hα 6563 Å near the loop footpoint. The top panel shows the variation of intensity, the wavelet power spectrum is given in the middle panel and the probability is given in the bottom panel. The light curve is from loop footpoint $(X, Y) =$ (58th pixel, 104th pixel) and is smoothed by window width 60.

the probability of ≈99–100 per cent (Fig. 3). It should be noted that we have chosen a box of width '4' at these locations to extract the light curves with good signal-to-noise ratios (S/N). Boxes with the width '4' have been chosen near the loop-top and footpoint with respect to their reference coordinates as mentioned in the figure captions of the wavelet diagrams. We extract maximum intensity from the chosen box. Our box of width '4' fits the loop dimension best. However, we have checked the results at other widths, e.g. '2', '3' and '6'. The boxes with width '2' and '3' still remain inside the loop dimension. However, the box with width '6' crosses the loop, which may not be appropriate especially near the limb where the background emissions and structures may be more effective compared to when it is far off the limb.

From the boxes of width '2' and '3', we get the same global periodicities at maximum power as we have obtained in the case of box width '4'. However, the power distribution in the intensity wavelet is slightly different for each case. This is obvious because we extract lower intensity with smaller box and higher intensity with larger box. We get a periodicity of ∼493 s and ∼587 s, respectively, near the loop footpoint and loop apex using the box of width '6'. The periodicity at apex is similar to the previous findings because the limb effects are not much far off the limb. The difference in the periodicity near loop footpoint shows the outside effects near the limb, which came into action due to the larger box size compared with the loop dimension. However, the similar periodicities (∼349 s near the footpoint and ∼587 s near the apex) with well-fitted or smaller boxes (of width '2', '3' and '4') clearly show that we are inside a well-isolated loop structure. However, we should take care of the dimension of the box during wavelet analysis especially near the limb. Thus, the selected loop intensities show the oscillations with significantly different periods near the apex (≈587 s) and footpoint (≈349 s), respectively. These observations may lead an interesting consequences for loop oscillation phenomena.

4 A THEORETICAL INTERPRETATION

The intensity oscillation with the period of $P_1 \approx 587$ s likely represents the fundamental harmonic of either fast sausage

(Nakariakov et al. 2003) or slow magnetoacoustic (Nakariakov et al. 2004) waves. The loop length is estimated as $L \approx 97$ Mm with corresponding phase speed as $2L/P_1 \sim 330$ km s^{-1}. The estimated phase speed is much higher than the sound speed corresponding to cool Hα line. Therefore, we suggest that the oscillation is due to a fast-sausage mode.

However, the dispersion relation of fast-sausage waves in straight coronal loop includes both trapped and leaky modes depending on the loop parameters (Edwin & Roberts 1983; Nakariakov, Melnikov & Reznikova 2003; Aschwanden, Nakariakov & Melnikov 2004). Due to low sound speed, we can easily use the cold plasma approximation. Hence, the cut-off wavenumber k_c is (Edwin & Roberts 1983; Roberts et al. 1984)

$$k = k_c = \left[\frac{v_A^2}{v_{Ae}^2 - v_A^2}\right]^{1/2} \frac{j_0}{a}, \quad (1)$$

where v_A and v_{Ae} are Alfvén speeds inside and outside the loop, a is the loop radius and $j_0 = 2.4$ is the first zero of the Bessel function J_0. The modes with $k > k_c$ are trapped in the loop, while the modes with $k < k_c$ are leaky. If we assume $B_0 = B_e$, then the cut-off wavenumber is (Aschwanden et al. 2004)

$$k_c = \left[\frac{1}{n_0/n_e - 1}\right]^{1/2} \frac{j_0}{a}, \quad (2)$$

where n_0/n_e is the electron density ratio inside and outside the loop. The width of selected loop can be roughly estimated as $2a \approx 6$ Mm. Hence, the trapped global sausage mode can be realized only if the density ratio is

$$\frac{n_0}{n_e} < \left(\frac{j_0}{\pi}\right)^2 \left(\frac{L}{a}\right)^2 \approx 600. \quad (3)$$

Thus, only very dense loop can support the non-leaky global sausage mode in the estimated length and width (Nakariakov et al. 2003; Aschwanden et al. 2004). The post-flare loops usually have a very high density contrast of the order of 10^2– 10^3. The selected loop is cool post-flare one, therefore the estimated density ratio falls in the expected range. Thus, the trapped sausage mode may occur in the loop, however wave leakage cannot be ruled out.

The fundamental harmonic of sausage oscillation has pressure anti-node at the loop apex (upper panel in Fig. 4). Therefore, it modifies the density leading to the intensity oscillation. However, it has pressure node at the footpoints, and should not lead to remarkable intensity oscillation. The observations show strong oscillations at the loop apex with the period of ≈587 s and almost no indication of the oscillation with this period near footpoint (see Fig. 2). Therefore, the oscillation with ≈587 s is probably due to the fundamental mode of sausage oscillations.

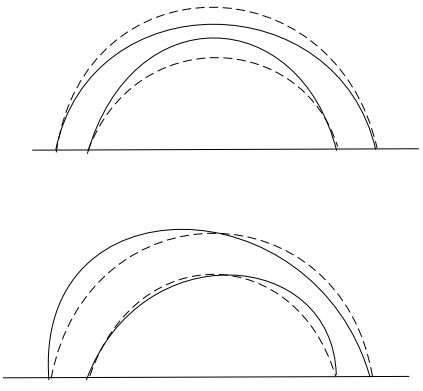

Figure 4. The fundamental (upper panel) and its first (bottom panel) harmonics of sausage oscillations in coronal loops.

On the other hand, the first harmonic of sausage oscillation has pressure node at the loop apex and anti-nodes at the mid-parts (lower panel in Fig. 4). Therefore, the first harmonic should show the intensity oscillation near the footpoint and almost no oscillation at the loop apex (see Fig. 3). Indeed, the oscillation with the period of ≈349 s has high probability near footpoint and no significant probability near the apex. Therefore, we interpret the oscillation with the period of ≈349 s as the first harmonic of fast-sausage waves in the coronal loop. In the curved geometry, this mode is identical to sausage swaying mode (Díaz, Zaqarashvili & Roberts 2006).

It must be mentioned that 349 s oscillation may be a consequence of non-linear excitation from the fundamental harmonic; however this possibility can be ruled out by two reasons. First, the amplitude of oscillation is not very strong and leaves a little space for non-linear interaction. Secondly, the period of the first harmonic is not exactly twice that of the period of fundamental mode, which was expected from the resonance condition.

As a consequence of above discussions, we suggest for the first observational evidence of the fundamental and its first harmonics of fast-sausage oscillations in cool post-flare loop.

4.1 The period ratio P_1/P_2 of fundamental and first harmonics

The ratio between the periods of the fundamental and the first harmonics of sausage waves is proportional to $P_1/P_2 \sim 1.68$, which is significantly shifted from 2. Similar phenomena were observed for fast-kink oscillations (Verwichte et al. 2004; De Moortel & Brady 2007; Van Doorsselaere et al. 2007). The deviation of P_1/P_2 from 2 in homogeneous loops is very small due to the wave dispersion (McEwan et al. 2006). But, longitudinal density stratification causes significant shift of P_1/P_2 from 2 (Andries et al. 2005; McEwan et al. 2006; Van Doorsselaere et al. 2007).

Using the results of Andries et al. (2005), we estimate the density stratification along the loop as $L/\pi H \approx 1.8$, where H is the density scaleheight. The calculation of McEwan et al. (2006) gives approximately the same value. Thus, both calculations yield the same density scaleheight as ∼17 Mm for the loop length of 97 Mm.

It must be mentioned that seismologically estimated scaleheight of 17 Mm is larger compared to the hydrostatical scaleheight at Hα temperature. This can be explained by two reasons. First, it is possible that the medium is not in equilibrium inside post-flare loops and, secondly, some mechanism (e.g. the variation of loop cross-section with height) other than the density stratification causes the deviation of P_1/P_2 from 2. Recently, Verth & Erdélyi (2008) have studied the effect of magnetic stratification on loop transverse kink oscillations and found that the loop divergence may have a significant effect on the period ratio almost similar to the density stratification. It would be interesting to study the effect of magnetic stratification on fast-sausage oscillations. However, even if the loop divergence effect reduces the estimated scaleheight to ∼7–8 Mm, it still remains larger than equilibrium scaleheight. Therefore, we suggest that the post-flare loops are not in equilibrium, which may cause plasma motions along the loop. In the footage of the observations, we clearly see the unidirectional mass motion from western footpoint to eastern footpoint in the selected loop which may indicate its departure from hydrostatic equilibrium. However, it will be interesting to further search the observational evidence in high-resolution space data. The question is open for further discussion.

4.2 Trapped or leaky mode?

It is not entirely clear from wavelet analysis that whether the global oscillation represents trapped or leaky mode. We see in Fig. 2 that the oscillation persists at least for 45 min, i.e. for ∼4–5 wave periods. However, the relative intensity plot in Fig. 2 (upper panel) likely shows that the oscillation amplitude decreases after 35 min. As intensity oscillations are due to the variation in plasma density, the decrement may reflect the process of wave damping. Since the oscillations are in sausage mode, the resonant absorption is unlikely to occur. Therefore, the wave leakage in the surroundings is the most probable candidate for the wave damping. If the oscillation represents the global leaky mode instead of the trapped one, then its phase speed would be close to the external Alfvén speed (Pascoe et al. 2007), which enables us to estimate its value as $v_{\rm Ae} = 2L/P_1 \sim 330\ \mathrm{km\,s^{-1}}$. However, this estimation is done for the straight magnetic cylinder, while noting that the curvature probably enhances the wave leakage (Verwichte, Foullon & Nakariakov 2005; Díaz, Zaqarashvili & Roberts 2006; Selwa et al. 2007).

For comparison, we may estimate the external Alfvén speed from the wave leakage in curved magnetic slab (Díaz et al. 2006). Using equation (25) of Díaz et al. (2006), we may write the expression for the external Alfvén speed as

$$v_{\rm Ae} \sim \frac{2a}{\pi^2 \tau_{\rm d}} \frac{n_0}{n_e},$$

where $\tau_{\rm d}$ is the damping time. From Fig. 2, we estimate the damping time as

$$\tau_{\rm d} \sim 20\ \mathrm{min},$$

then using the density ratio of $n_0/n_e \sim 600$ we estimate the value of the external Alfvén speed as $v_{\rm Ae} \sim 300\ \mathrm{km\,s^{-1}}$ [note that this estimation is done for a curved slab, therefore equation (3), which is obtained for a straight loop, is not valid here].

5 DISCUSSION AND CONCLUSIONS

Using high spatial (1.3 arcsec) and temporal (5 and 10 s) resolution Hα observations, we found intensity oscillations with different periodicity in different parts of cool post-flare loop. The intensity shows the oscillation with the period of ≈587 s at the loop apex and with the period of ≈349 s near loop footpoint. We interpret the oscillations as signature of the fundamental and first harmonics of the fast-sausage mode. It is difficult to say whether the oscillations are due to the trapped or leaky modes. However, intensity plot likely shows the decrement of the oscillation amplitude, therefore we suggest the presence of leaky nature of these modes. Seismologically estimated Alfvén speed outside the loop is ∼300–330 $\mathrm{km\,s^{-1}}$. Using the period ratio P_1/P_2, we also estimate the density scaleheight in the loop as ∼17 Mm. This value is much higher than the equilibrium scaleheight at low Hα temperature, therefore we suggest that cool post-flare loops are not in hydrostatic equilibrium. In the footage of the observations, we clearly see the unidirectional mass motion from western to eastern footpoint in the selected loop which indicates its departure from hydrostatic equilibrium.

In conclusion, we report the first observational evidence of multiple oscillations of the fast-sausage modes in cool chromospheric post-flare loop. Future detailed observational search should be investigated, especially using recent space-based observations.

ACKNOWLEDGMENTS

AKS wishes to express his gratitude to Professor Ram Sagar (Director, ARIES) for his valuable suggestions and encouragements and to Dr E. O'Shea for the providing wavelet tool. TVZ acknowledges the Georgian National Science Foundation for the financial support through its grant GNSF/ST06/4-098. We wish to express our gratitude to the anonymous referee for his valuable comments that considerably improved our manuscript.

REFERENCES

Andries J., Arregui I., Goossens M., 2005, ApJ, 624, L57
Ali S. S., Uddin W., Chandra R., Mary D. L., Vrsnak B., 2007, Sol. Phys., 240, 89
Aschwanden M. J., Fletcher L., Schrijver. C. J., Alexander D., 1999, ApJ, 520, 880
Aschwanden M. J., Nightingale R. W., Alexander D., 2000, ApJ, 541, 1059
Aschwanden M. J., Nakariakov V. M., Melnikov V. F., 2004, ApJ, 600, 458
De Moortel I., Brady C. S., 2007, A&A, 664, 1210
Díaz A. J., Zaqarashvili T. V., Roberts B., 2006, A&A, 455, 709
Edwin P. M., Roberts B., 1983, Sol. Phys., 88, 179
Joshi A., Chandra R., Uddin W., 2003, Sol. Phys., 217, 173
Linnell Nemec A. F., Nemec J. M., 1985, AJ, 90, 2317
McEwan M. P., Donnelly G. R., Díaz A. J., Roberts B., 2006, A&A, 460, 893
Nakariakov V. M., Ofman L., 2001, A&A, 372, L53
Nakariakov V. M., Melnikov V. F., Reznikova V. M., 2003, A&A, 412, L7
Nakariakov V. M., Tsiklauri D., Kelly A., Arber T. D., Aschwanden M. J., 2004, A&A, 414, L25
Nakariakov V. M., Ofman L., DeLuca E. E., Roberts B., Davila J. M., 1999, Sci, 285, 862
O'Shea E., Banerjee D., Doyle J. G., Fleck B., Mugtagh F., 2001, A&A, 368, 1095
O'Shea E., Srivastava A. K., Doyle J. G., Banerjee D., 2007, A&A, 473, L13
Pascoe D. J., Nakariakov V. M., Arber T. D., 2007, A&A, 461, 1149
Roberts B., Edwin P. M., Benz A. O., 1984, ApJ, 279, 857
Selwa M., Murawski K., Solanki S. K., Wang T. J., 2007, A&A, 462, 1127
Srivastava A. K., Kuridze D., Zaqarashvili T. V., Dwivedi B. N., 2008, A&A, 481, L95
Torrence C., Compo G. P., 1998, Bull. Am. Met. Soc., 79, 61
Van Doorsselaere T., Nakariakov V. M., Verwichte E., 2007, A&A, 473, 959
Verwichte E., Foullon C., Nakariakov V. M., 2005, A&A, 446, 1139
Verwichte E., Nakariakov V. M., Ofman L., Deluca E. E., 2004, Sol. Phys., 223, 77
Verth G., Erdélyi R., 2008, A&A, in press
Wang T. J., Solanki S., 2004, A&A, 421, L33

This paper has been typeset from a TEX/LATEX file prepared by the author.